Expected performances for a 2-μm differential absorption lidar using new HgCdTe avalanche photodiodes

Arnaud Dumas

Mai 2014

Supervisors :

- Fabien Gibert (Laboratoire de Météorologie Dynamique, Ecole Polytechnique, CNRS, Palaiseau)

- Johan Rothman (CEA/LETI, Campus Minatech, Grenoble)

Examinator :

- Fredrik Laurell (Laser physics department, KTH, Stockholm)

Abstract

Differential absorption lidar (DIAL) is an active remote sensing technique, which has been developed to monitor trace constituents such as greenhouse gases over distances that range from hundreds of meters to tens of kilometers in the atmosphere. A DIAL lidar dedicated to CO_2 probing in the atmospheric boundary layer has recently been developed at Laboratoire de Météorologie Dynamique (IPSL, France). This so-called COWI[1] lidar relies on a 2μm Ho:YLF solid state laser and coherent detection. In case direct detection is used, performance on measurement strongly depends on detector performance. That is why recent advances in the field of HgCdTe avalanche photodiodes (APD) - which achieve remarkable low levels of noise along with high gains in the considered spectral surrounding - open the way to outstanding precision in atmospheric probing around 2μm. The aim of this study is to estimate the performance of DIAL lidar using such APDs in the framework of atmospheric CO_2 probing.

---

[1]for CO_2 and wind

Introduction

The word **lidar** refers to the acronyme Light Detection And Ranging. It is a radar-like method[2] using a laser : a laser beam is emitted towards a target, the target is stimulated by the laser ray and produces some radiations that are partially collected and analyzed to evaluate some features of the target. The development of the first lidars came along with the development of the first lasers in the sixties. The first lidar atmospheric measurements were published in 1963 and less than ten years later, all basic techniques on lidar had been demonstrated. Since then, improvements on lidars are mostly related to technological advances in laser systems, optical components and electronic devices (see [7], Ch1, p1-3 for a deeper introduction to lidar history).

Fifty years after the first measurements with a ruby laser, lidars are nowadays commonly used for a wide range of applications. To name only a few of them : ozone layer monitoring, study of stratospheric volcanic aerosols, air pollution monitoring within the atmospheric boundary layer, bathymetry, evaluation of wind velocity for windmill yield optimization. It has to be mentioned that if the first lidars were operated from ground, the development of airborne and space lidars has considerably extended their range. The LITE mission funded by NASA (Lidar In-space Technology Experiment) was launched in 1994 and turned out to be a tremendous scientific success, confirming lidar outstanding potential for space measurements. To get more details about airborne/space lidars history, see [7] (Ch13, p 355-391).

In the prospect of climate change modeling, as CO_2 stands for the most important contributor to global warming among greenhouse gases, the need for well sampled global CO_2 measurements has become crucial for a thorough understanding of carbon cycle, ie to identify sources, sinks and transport features. Such measurements are already available through passive techniques and in-situ instrumentation. However, in-situ measurements are too sparse and passive measurements often suffer from a lack of accuracy. This is the main motivation for the development of CO_2 lidars, which should be able to provide routine high accuracy CO_2 measurements, either from ground

---

[2]that is why lidar is often called laser radar

3

of from space (see [2], Introduction, p 1-4).

In our study, we focus on a method called **differential absorption lidar** (DIAL), which can be applied to measure atmospheric CO_2 mixing ratio. Such a method has already been successfully used by several science teams around the world to monitor CO_2. However, improvements are still needed to meet the required performances for specific applications such as derivation of CO_2 turbulent flows, which are of huge interest for our understanding of CO_2 exchange processes at the bottom/top of the atmospheric boundary layer. For this reason, lidar community is steadily looking for new optical components or electronic devices that achieve higher performances.

Avalanche photodiodes (APDs) are not a brand new technology. They are part of the microelectronic revolution that occurred in the sixties with the development of semiconductor physics. Yet the real potential of HgCdTe APDs was only revealed in the very late nineties, when american instrumentalists discovered that despite of model predictions, considerable gain was achievable with reasonable noise amplification. The french agency CEA[3] started to investigate the field in 2005 and by now maturity is almost reached for these components, which are to be tested for laser telecommunications, imaging and remote sensing within coming months.

This study aims at estimating the performances of DIAL lidar using such HgCeTe APDs. Indeed preliminary characterization of HgCdTe APDs has been carried out in Grenoble and we combine these experimental results with a DIAL instrumental simulator. Thus, we first recall the basics on lidar system and relevant physics. In a second part we introduce mathematical background and derive the lidar equation. In a third part we describe the DIAL method. In a fourth part, we present the HgCdTe APDs and their performances. Finally, using the equations derived in the second and third parts, we present a simple lidar simulator and expected results in the framework of atmospheric CO_2 mixing ratio measurements.

---

[3]Centre à l'Énergie Atomique

Contents

1 Atmospheric Lidar

In this first part, we introduce gradually basic knowledge on lidar - skipping many details on purpose - it is intended to provide the reader with an overview of instrument features, typical values of parameters and relevant physics.

1.1 Lidar setup

Any lidar system basically consists in three subsystems :

☞ emission subsystem : pulsed laser, output monitor, optical components, beam expander.

☞ receiver subsystem : telescope, optical components, spectrum filter, photodetector.

☞ signal processing subsystem : analog digital converter, acquisition card, data processor, display monitor.

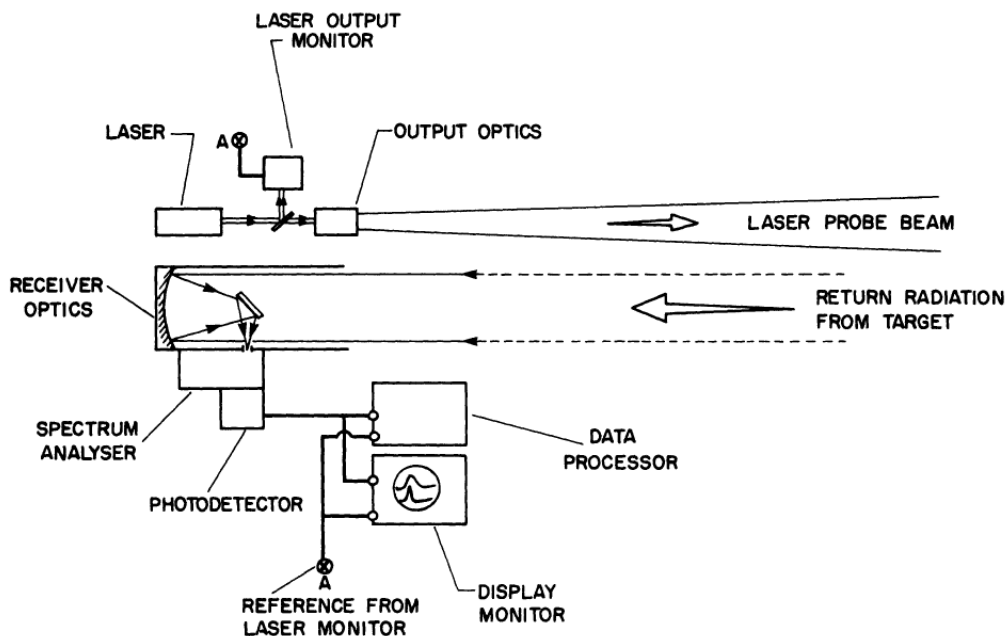Slightly different setups are possible. Fig 1 provides a representative scheme.

Figure 1: Essential elements of a lidar system (Taken from [4], p 214).

1.2 Lidar key parameters

We describe here the main lidar parameters and give some insight on how they impact the measure.

Laser wavelength. The laser beam is almost monochromatic and the choice for λ - the wavelength - is motivated by the desired application, given that the interaction between the laser light and the atmospheric components strongly depends on λ^4. Moreover, the range of possible λ depends on the chosen[5] laser technology. For instance, solid state laser spectral range is narrow. On the contrary, optical parametric oscillators (OPO) spectral range is much larger.

Pulse length and energy. For most atmospheric applications, pulsed lasers are used. The typical pulse length is around 10-100 nanoseconds and the pulse energy ranges from 10μJ to 100 mJ. Using very short pulses allows to perform range-resolved measurements. Assume dirac pulse emitted at time $t = 0$ and consider Fig 2, time t and range R are connected by $2R = ct$ where R is the range of the target plane and t the time at which the signal reaches the detector.
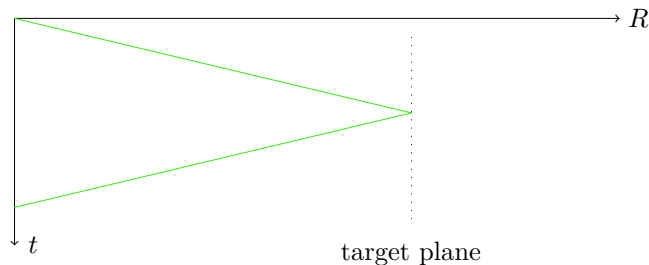

Figure 2: For a pulse emitted at $t = 0$, propagating at constant velocity c, The signal detected at time t comes from the plane located at range $R = \frac{ct}{2}$

Pulse repetition frequency. The PRF is about 1-1000 Hz. An important assumption is that shots are independent. By independent, we mean that the photodetector only receives contribution from one shot at a time. For instance if a pulse is emitted à time $t = 0$,

---

[4]this will be detailed later

[5]and existing!

it will only contribute to the receiver signal over the period $[0, \Delta t]$ where $\Delta t = 1/\text{PRF}$. This assumption holds because the signal drops very quickly as we will see later. Notice that for a PRF of 1000 Hz, Δt is equal to 1 ms - corresponding to a maximum probing distance $R = \frac{c\Delta t}{2}$ of 150 km.

Telescope diameter. This latter ranges from a few centimeters (10cm) to a few meters (1-3m). The larger the telescope, the larger the number of photons that are collected. However there are limitations in several cases - small detector, non isotropic scattering - that we will not discuss here.

Optical efficiency. This term refers to the efficiency of all optical components such as polarizers, lenses, optical fibers, mirrors. Usually its value is limited to a few percents, typically 5%.

Photodetector performances. In the framework of atmospheric lidar applications, the signal strength varies of several orders of magnitude. As a consequence, high precision detectors are required. By high precision, we mean detectors that achieve very low noise levels. One should keep in mind that every technology is applicable in a certain spectral range, meaning that detector performances are significantly different depending on spectral position. On top of precision, other important requirements are : linearity of the gain, spatial homogeneity, suitable bandwidth.

Sampling rate. It is the frequency for data acquisition, whose value is typically around 100MHz. This corresponds to $\Delta t = 10^{-8}$s or $\Delta R = 1,5$m.

In table 1 we present the features of the COWI[6] lidar that is currently developed at IPSL, Laboratoire de Météorologie Dynamique, Palaiseau (France).

---

[6]for CO_2 and Wind

Parameter	Value
Wavelength λ	2051 nm
Pulse length τ	50 ns
Pulse energy E	10 mJ
Pulse Rate Frequency (PRF)	2 kHz
Telescope diameter	10 cm
Sampling rate	400 MHz

Table 1: COWI lidar parameters (2014).

1.3 Light-matter interaction in the atmosphere

There are many physical processes involved. We focus here on elastic scattering and absorption because they are the one used in DIAL technique. Elastic means that the scattered radiation has the same frequency as the incident radiation. An exhaustive description of different sorts of scattering is available in [4] (Ch 6, p 206-207).
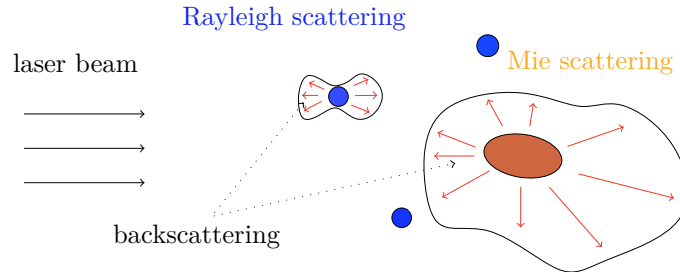

Figure 3: Different sorts of scattering occur. Molecular scattering is due to nitrogen, oxygen, carbondioxide, H_2O, etc. Particular scattering is due to aerosols such as pollutants, pollens, volcanic ashes, clouds, desertic dusts, etc.

1.3.1 Elastic scattering

Regarding atmospheric elastic scattering, there are two classic theories : **Rayleigh scattering** and **Mie scattering**. The first one concerns atoms and molecules : the incident radiation is an polarized oscillating electromagnetic field $\overrightarrow{E}$, which forces the electrons of the atoms, molecules to oscillate, producing in turn a radiation with same

frequency in every direction, with variable intensity though. Mathematical developments are provided in [4] (Ch 2, p38-47). The second one covers the issue of scattering of a radiation by spherical objects, which can be applied either molecules or particles. However, in every day life Mie scattering usually refers to particle scattering. We call backscattering the fraction or scattered radiation that heads in the opposite direction to the laser beam direction. Backscattered radiation are collected in the receiver (see Fig 3).

Besides, it has to be mentioned that - in Near Infrared Region - molecular scattering intensity is much lower than particular scattering. The reason for that is the Rayleigh scattering dependency with respect to λ, that is proportional to $1/\lambda^4$. On the contrary, Rayleigh scattering is predominant in Ultra Violet Region. This point is of special importance when considering vertical structure of particles mixing ratio and backscattered signal in near infrared region (see Fig 4).
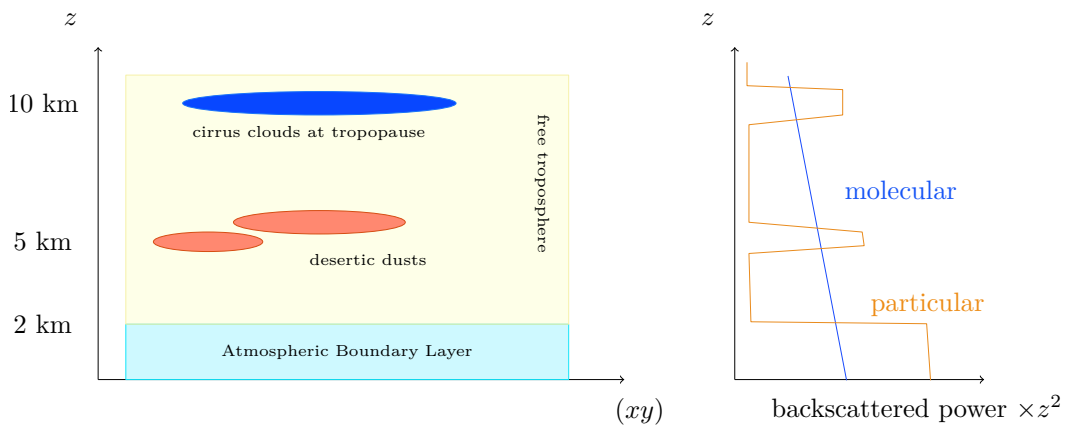

Figure 4: An atmospheric structure example and corresponding backscattered signal in Near Infrared Region. Most of particles are confined below the top of the atmospheric boundary layer ($\approx$ 1,5-2 km) but specific structures such as cirrus clouds or desert dusts exist upper in the free troposphere. These structures backscatter an large part of the incident power, making them easy to detect with lidar. Generally speaking, molecular signal is much harder to capture.

1.3.2 Absorption

Absorption occurs when the frequency of the laser beam matches to the absorption band of an atmospheric molecule - for instance CO_2,

H_2O, N_2, O_2. In quantum physics theory, it corresponds to the transition between different levels of energy of the molecule (see Table 2). Around $\lambda = 2\mu m$, there are mainly CO_2 and H_2O absorption bands.
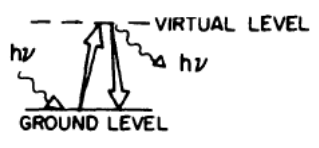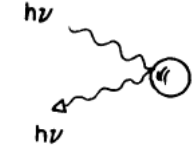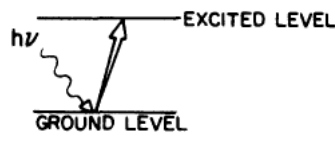
Rayleigh scattering	Mie scattering	Absorption

Table 2: Adapted from [4] (Ch 6, P 206).

2 The lidar equation

In this second part, we introduce the mathematical objets corresponding to the physical processes described in part one. We derive the the lidar equation and comment on it.

2.1 Electromagnetic energy flows

2.1.1 Irradiance

The term **irradiance** refers to a flow of electromagnetic energy per unit time per unit surface ($J.s^{-1}.m^{-2}$). Define $I(R, \overrightarrow{r})$ - the laser irradiance at range R and position $\overrightarrow{r}$ (see Fig 5).
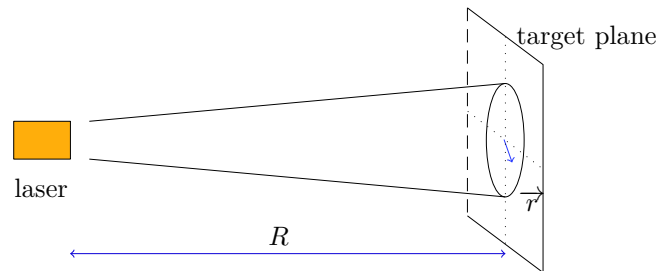

Figure 5: The laser beam section in the target plane defines an area whose infinitesimal elements dS receive a power $I(R, r) \cdot dS$.

2.1.2 Radiance

Consider now a small surface element dS of source and $\overrightarrow{n}$ an unit vector perpendicular to this surface. Define the radiance $J(R, \overrightarrow{r})$ as the flow of electromagnetic energy per unit solid angle per unit projected area. Thus the power emitted from dS into solid angle $d\Omega$, centered about an angle θ from the normal is $J(R, \overrightarrow{r})dS\cos(\theta)d\Omega$ (see Fig 6)
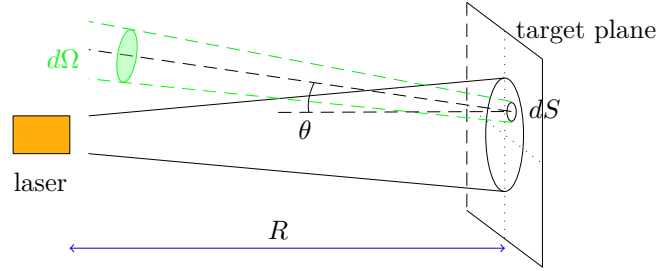
Figure 6: Radiance from a small surface element dS.

Hence, introducing A - the receiver area - that we assume centered about the laser axis, the solid angle Ω corresponding to a surface seen at range R with angle θ is $\Omega = \frac{A}{R^2}\cos(\theta)$.

Figure 7: Radiance from dS reaching the receiver.

Summing the contributions of all small surface elements of surface S, we get the power received on the area A :

$$\frac{A}{R^2} \cdot \int_S J(R, \overrightarrow{r})\cos(\theta(\overrightarrow{r}))^2 dS \tag{1}$$

Remark. We made an important assumption : we considered that the small surface elements were incoherent. This hypothesis allows us

to sum easily. However, this assumption does not always hold. See the discussion between direct and coherent detection.

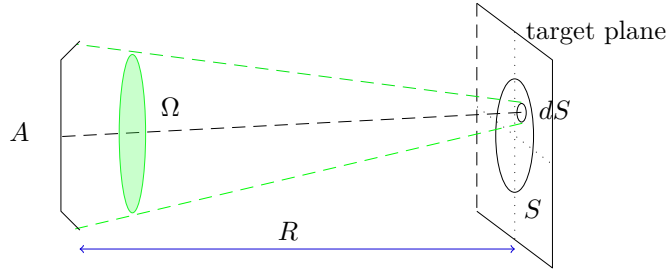## 2.2 Laser beam attenuation

2.2.1 Scattering

Due to absorption and scattering, the laser beam is attenuated while moving forward. We introduce the scattering coefficient $\alpha_s(R)$, the absorption coefficient $\alpha_a(R)$ and we assume a Beer-Lambert law

$$dP = -(\alpha_s(R) + \alpha_s(R))P(R)dR$$

where $P(R)$ is the laser beam power at range R. As a consequence, the laser beam attenuation over $[0, R]$ is

$$T(R) := \exp\left(-\int_0^R \alpha_s(x) + \alpha_a(x)dx\right)$$

where $\int_0^R \alpha_s(x) + \alpha_s(x)dx$ is called the **optical depth**. Assuming very small laser beam divergence, we can write :

$$\int I(R, \overrightarrow{r})dS = T(R) \cdot \int I(0, \overrightarrow{r})dS$$

2.2.2 Backscattering

In the last section, we introduced the global scattering coefficient α_s. Let β_π be the backscattering coefficient, ie the ratio of backscattered radiation per unit solid angle. In common assumption is $\beta_\pi = k\alpha_s$ with $k = 0{,}01\text{-}0{,}1$. However, even if β_π and α_s variations are linked, this assumption does not hold generally speaking. We can now use β_π to link the irradiance on a small surface element dS to the backscattered radiance.

$$J(R, \overrightarrow{r}) = \beta_\pi(R) \cdot I(R, \overrightarrow{r})$$

2.3 Simple form of the lidar equation

From equation (1) - assuming that the laser pulse is a dirac[7] emitted at time $t = 0$ - the power received on the receiver area A at time t is

$$D(2R/c) := \frac{A \cdot T(R)}{R^2} \cdot \int_S \beta_\pi(R) \cdot I(R, \overrightarrow{r}) dS$$

Thus it comes

$$D(2R/c) = \frac{A \cdot T(R)^2}{R^2} \cdot \beta_\pi(R) \cdot \frac{E}{\tau} \tag{2}$$

Notice the square for the factor $T(R)$. It comes first from the fact that the laser beam comes from the laser to the target plane and then from the target plane to the receiver.

In the previous equation, we have assumed that :

☞ pulses could be considered as diracs.

☞ laser light was purely monochromatic.

☞ all backscattered light in the solid angle A/R^2 was collected by the receiver.

Depending on the situation, some of those assumptions may not hold. A more thorough expression is derived in [4] (Ch 7, p 239).

3 The DIAL technique

3.1 Principle

The DIAL technique was developed to perform mixing ratio measurements of trace constituents in the atmosphere such as greenhouse gases. This technique relies on spectroscopic properties of the constituent. The idea is to use two wavelengths - usually so-called ON and OFF - for which the absorption will be different.

---

[7]In pratice, the pulse length τ is about 50 ns, which corresponds to a layer of 7,5 m. A current assumption to simplify the calcula is that the atmospheric variables are constant over 50 ns periods or in an equivalent way constant over layers of several meters - ie that the medium is homogeneous. If we assume on top of that, that a rectangular pulse of constant power E/τ and length τ, then obtain equation 2.

DIAL principle. for two laser shots performed at the same time, one at λ_{ON} and one at λ_{OFF}, the difference between the backscattered signal of the two shots in only imputable to CO_2 absorption, whatever the atmospheric conditions are, whatever other physical phenomena such as multiple scattering, depolarization, etc. that may modify the signal. For this latter reason, the method is called auto-calibrated.

If we write the equations derived in the previous section (eq 2)-adding an optical efficiency factor K - for the backscattered optical power P, we get :

$$P_{ON}(R) = K_{ON} \frac{A \cdot T_{ON}(R)^2}{R^2} \cdot \beta_{\pi(R),ON} \cdot \frac{E}{\tau}$$

$$P_{OFF}(R) = K_{OFF} \frac{A \cdot T_{OFF}^2}{R^2} \cdot \beta_{\pi,OFF}(R) \cdot \frac{E}{\tau}$$

Applying the DIAL principle is equivalent to assume that $K_{ON} = K_{OFF}$ and $\beta_{\pi(R),ON} = \beta_{\pi(R),OFF}$. It comes

$$\frac{1}{2} \cdot \ln\left(\frac{P_{OFF}}{P_{ON}}\right) = \int_0^R \alpha_{a,CO_2,ON} - \alpha_{a,CO_2,OFF}(x) dx$$

Therefore

$$\boxed{\Delta \alpha_{a,CO_2}(r) = \frac{1}{2} \cdot \frac{d}{dR} \ln\left(\frac{P_{OFF}}{P_{ON}}\right)}$$

The last step is to derive carbondioxide mixing ratio from the quantity $\frac{1}{2} \cdot \frac{d}{dR} \ln\left(\frac{P_{OFF}}{P_{ON}}\right)$, which is directly readable from lidar measurements. Recall that by definition, the absorption coefficient is related to absorption cross section via :

$$\Delta \alpha_{a,CO_2}(r) := N_{CO_2} \cdot \Delta \sigma_{a,CO_2}$$

where N_{CO_2} is the concentration of CO_2 molecules at range R and σ_{a,CO_2} is the absorption cross section at range R. Thus if we know the absorption cross sections σ_a we can retrieve N_{CO_2}. Finally as $N_{CO_2} = X_{CO_2} N_{dryair}$ where X_{CO_2} is the carbon dioxide mixing ratio at range R, we get :

$$\boxed{X_{CO_2} = \frac{1}{N_{dryair}} \cdot \frac{1}{\Delta \sigma_{a,CO_2}} \cdot \frac{1}{2} \frac{d}{dR} \ln\left(\frac{P_{OFF}}{P_{ON}}\right)}$$

Important remark. The quantity stated above assumes dry air. To perform precise measurements, the water vapor must be known with good precision and the above expression corrected - taking into account water vapor mixing ratio.

3.2   Spectroscopy

In the previous section, we have explained a very important point : DIAL measurements rely on both lidar backscattered power measurements and knowledge of the absorption cross section profile along the lidar shooting line. The absorption cross section is obtained via spectroscopy.
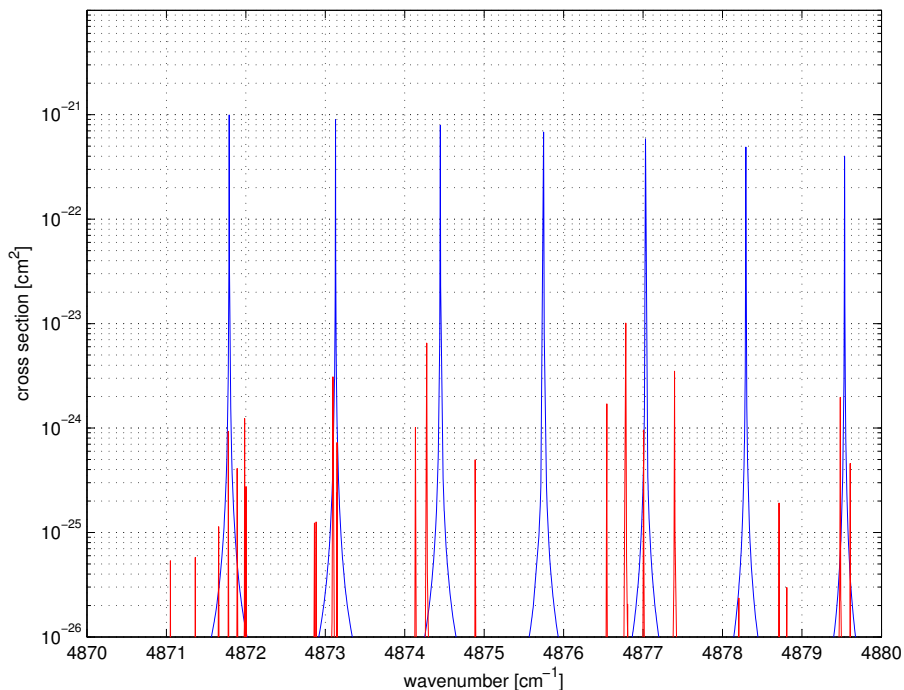

Figure 8: CO_2 (blue) and H_2O (red) absorption cross sections around wavelength 2 μm.

Below $z = 10$ km, in Near Infrared Region, lorentzian profile[8] is usually used to approximate the molecular absorption cross section dependency with respect to temperature and pressure. We have :

$$\sigma_a = \frac{S}{\pi \gamma_c} \cdot \frac{1}{1 + \left(\frac{\nu - \nu_0}{c \gamma_c}\right)^2}$$

---

[8]broadening is mainly caused by collisions between molecules

where S is the intensity of the line and γ_c is the air broadening pressure halfwidth (HWHM). These two quantities depend on temperature and pressure. Their expression can be found in [3] (p111). Having retrieved the parameters values from the spectroscopic database GEISA, we were able compute and plot the absorption cross section versus the frequency (see Fig 8).
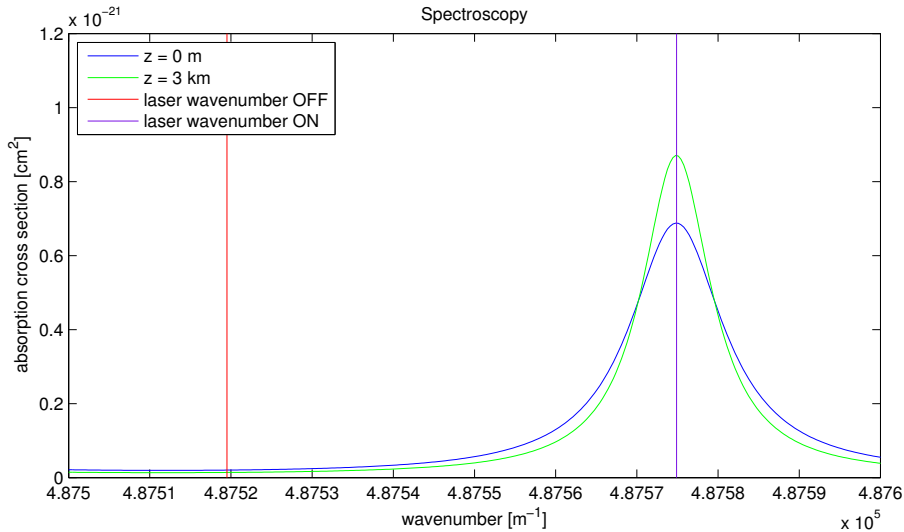

Figure 9: An example for the choice of k_{ON} and k_{OFF}, which corresponds to $\lambda_{ON} = 2050, 967$ nm (this line is the one currently used for COWI lidar) and $\lambda_{OFF} = 2051, 2$ nm. Notice the change in the line profile depending on altitude.

In the following we explain the choice of the wavelengths ON and OFF. The first step is to choose a CO_2 absorption line. The important parameters for this choice are :

☞ the line must only belong to CO_2 absorption spectrum. Indeed we want CO_2 to be the only constituent accounting for absorption. Around 2 μm, there are also many H_2O absorption lines. Although H_2O absorption cross sections in this spectral region are smaller (of about two orders of magnitude - see Fig 8), H_2O absorption over an atmospheric column is comparable as H_2O mixing ratio in the atmosphere is about 1% while CO_2 mixing ratio is only 0,04%.

☞ the central wavenumber of the line should be independent with respect to temperature. The reason for this is that we must know precisely the CO_2 absorption cross section throughout the atmo-

17

sphere (Dependency of the line profile with respect to temperature, pressure are detailed in the next section).

The second step is to choose two wavenumbers : the first one is usually taken at the center of the chosen absorption line and the second wavenumber, in a position where the absorption is almost zero. The two chosen wavenumbers are called respectively ON and OFF and a typical example is pictured in Fig 9.

4 HgCdTe Avalanche Photodiodes

Having presented the lidar instrument and DIAL principle in the previous sections, we focus in this part on the features of the HdCdTe APDs[9].

4.1 Avalanche Photodiodes

In a photodiode, a photon whose energy matches the gap of the semiconductor-based photodiode entails the generation of an electron-hole pair. This latter - depending on bias or not - produces either a tension or a current. The basic idea of APDs is that the number of such electron-hole pairs (generated with a constant number of incident photons) can be increased through a physical phenomenon called impact ionization (see Fig 10). The interested reader will find a thorough explanation in [1] (Complement 6.C). HgCdTe APDs amplification features are close to optimal :

☞ linear gain which is an exponential function of reverse bias

☞ close to zero excess noise

☞ response time close to independent of gain

☞ close to constant signal to noise ratio

Avalanche Photodiodes (APDs) are widely used to detect small signals. There are especially adapted for laser remote sensing. Developments in APDs come along with developments in semiconductor materials. For this reason, different APDs technologies do not have

---

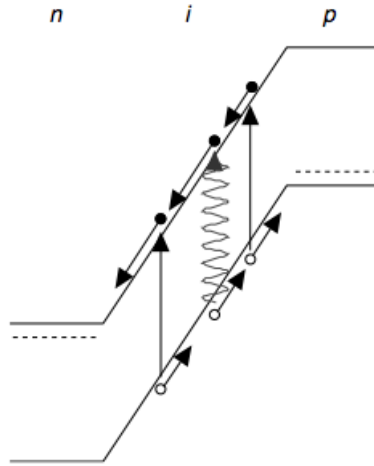[9]Also sometimes called MCT APDs - for Mercury, Cadmium, Tellure

Figure 10: Taken from [1]. In an avalanche diode, a photogenerated electron-hole pair creates secondary pairs by impact ionization.

the same level of maturity. For instance, InGaAs APDs have been used for a long time for detection around $1,5\mu$m. On the contrary HgCdTe APDs development started later (in the early 2000s) and allow detection until 4 μm. State of the art results were presented at OPTRO 2014[10] by Johan Rothman[11]. See [6]. In the following we present the most important results - both simulated and experimental - related to these detectors.

4.2 Instrumental setup

To measure the performances of the APD, it was coupled with a transimpedance amplifier (TIA) to reach reasonable tension values. A basic scheme of the instrumental setup is presented in Fig 11.

4.3 Simulations

In a first part, we present simulations of the behaviour of the APD - namely dependency of gain and noise equivalent power with respect to reverse bias at constant temperature and dependency of gain and noise equivalent power (NEP) with respect to temperature at constant reverse bias. These simulations assume ideal features of the APD and ideal environment. We will see in a second part that experimental data

---

[10]6th International Symposium on Optronics in Defence and Security, Paris, January 2014

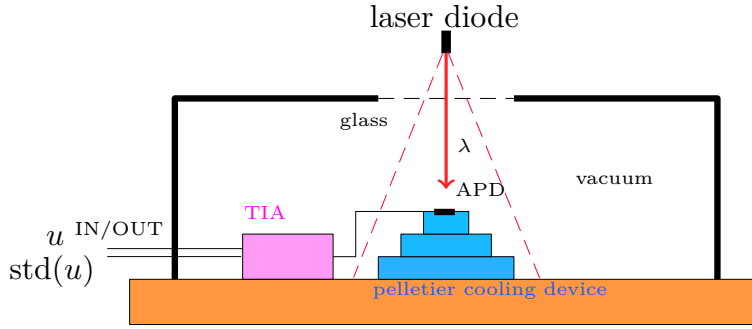[11]Centre à l'Energie Atomique (CEA/LETI), Minatech Campus, Grenoble

Figure 11: The standard box for APD testing. A diode laser at 1,55 μm whose power is known is used. The fraction of light that reaches the APD has been calculated with geometrical considerations assuming gaussian beam. As a consequence we know the incident optical power on the detector. Besides, we measure the signal voltage u at the output of the TIA and its standard deviation std(u). The APD is kept at 181 K approximately thank to a TEC cooling system.

suffer from non ideal environment. Still the simulations provide us with a good idea of the orders of magnitude of the different parameters and their best expected values.

A model for APD performance prediction was developed at CEA/LETI for such a setup[12]. The aim is to estimate the gain M given the Cadmium ratio, the operating temperature T and the APD bias V.

Given the set of parameters of Table 3 and given M thanks to our numerical model, we are able to compute the Noise Equivalent Power (NEP) which is defined as the incident required power so that the Signal to Noise Ratio equals 1. The dark current was estimated from experimental measurement[13].

Thus,

$$NEP = \frac{\sqrt{i_{TIA}^2 + 2eM^2FI_d}}{M} \cdot \frac{hc}{\lambda} \cdot \frac{1}{e} \cdot \frac{1}{\eta}$$

where i_{TIA} is the incident current on the TIA [A/$\sqrt{Hz}$], M the APD gain, η the quantum efficiency, F is the excess noise factor and e the elementary charge. In the previous equation, the last part is only a conversion from an electric current to a photon rate. The first part includes noise from the APD dark current and noise from the TIA,

---

[12]Because of confidentiality terms, the model was not detailed in any way.

[13]Such a measurement is far from being a trivial experiment. Indeed to make sure that there is no infrared incident light on the APD, we must be sure that any device in the near environment of the detector is cooled at low temperature.

which is supposed to be known. We basically sum the variances of the different noises. The factor $1/M$ is due to the fact that the NEP is defined as the equivalent to noise *incident* optical power, that is to say before amplification of factor M. Same thing for $\frac{1}{\eta}$.

Parameter	Value
Wavelength λ	1,55 μm
Surface	$1 \cdot 10^{-8}$ m^2
Quantum Efficiency (η)	0.8
Excess noise factor (F)	1.3
TIA noise	$1 \cdot 10^{-12}$ A/$\sqrt{\text{Hz}}$

Table 3: Parameters for instrumental setup presented in Fig 11.

We also define $NEPh$ as the number of photons equivalent to noise accumulated during characteristic time $TC = \frac{1}{2BW}$ where BW is the bandwidth of the system. Hence,

$$NEPh = \frac{NEP}{h\nu} \cdot \sqrt{BW} \cdot TC$$

Now, we present numerical results for the estimated NEP at $T = 180$ K and for different values of V. See Fig 12. Consider also numerical results for several operating temperatures given bias $V = 14V$. See Fig 13.

Remarks.

☞ APD behaviour is very sensitive to temperature. To reach low noise levels, it is very important to have a cooling system able to stabilize the system at low temperature.

☞ APD gain is reaching very important values for high bias. However the risk of damage is also more important for high bias. A study on reliability of such APDs is to carried out in the future.

☞ For low gain, ie for low bias, performance (NEP) is limited by the TIA noise. For high gain, we start noticing limitation due to APD dark current.
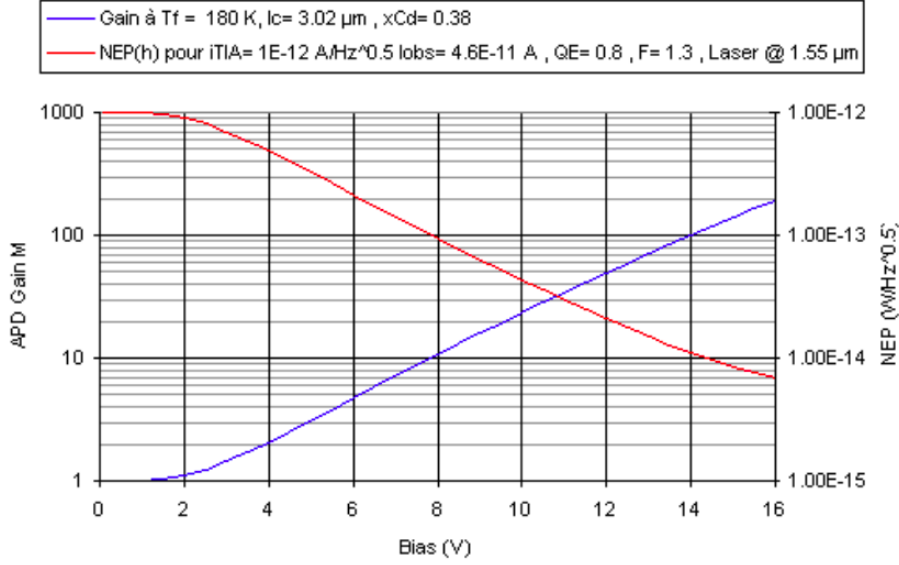
Figure 12: Estimation of NEP and Gain as functions of bias. Simulated results.

4.4 Experimental results

In this second part, the numerical results presented in the previous section are here confronted with experimental measurements performed at CEA/LETI. The experimental setup is the one presented in Fig 11. For several bias, we measured the tension u behind the TIA as well as its standard deviation std(u). As we know its gain - $G_{TIA} := 350000$ V/A - we were able to compute the product $\eta \cdot M$ where M is the APD gain :

$$M \cdot \eta = \frac{u}{P_{incident}} \cdot \frac{hc}{\lambda e} \cdot \frac{1}{G_{TIA}}$$

Finally the NEP was estimated with a bandwidth of 14,5 MHz through the formula

$$NEP = \frac{u}{G_{TIA} \cdot \eta \cdot M} \cdot \frac{hc}{\lambda e} \cdot \frac{1}{\sqrt{BW}}$$

Data are gathered in table 4 and experimental points are pointed out in green in Fig 14.

Important remarks.

☞ The measurements presented in table 4 were performed around $T = 181$K. Still it has to be mentioned that despite numerous
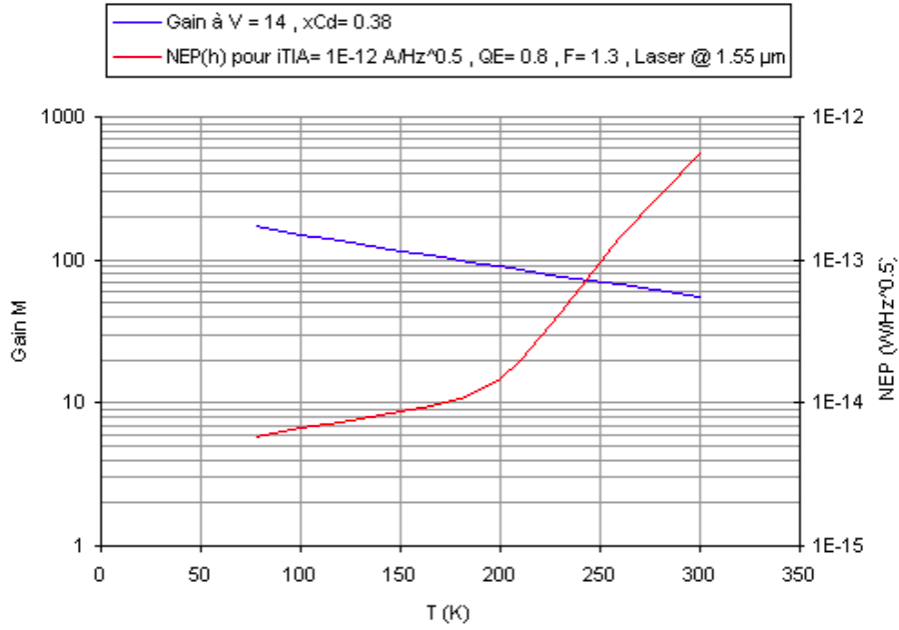
Figure 13: Estimation of NEP and Gain as functions of temperature. Simulated results.

efforts to ensure optimal cooling, the reached operating temperature was not fully stable. We indeed observed a rise of several degrees (5-10) over 1 hour of operation.

☞ The measured current without the laser diode was about 2 nA. This means that on top of the dark current, some additional current - probably due to infrared thermal radiations in the near environment - was increasing the noise. Further optimization using a cold screen to reduce this thermal noise are to be carried out.

Incident power (nW)	u (mV)	$M \cdot \eta$	**Std**(u) (mV)	**NEP** (fW/$\sqrt{Hz}$)
4.98	1,98	0,91	1,89	1249,1
4.98	21,1	9,68	1,92	119,1
4.98	44,1	20,23	2,18	64,7
4.98	83,7	38,39	2,89	45,2

Table 4: Experimental Data for Gain & NEP.

☞ The quantum efficiency is a bit high (0,91 : first row where M=1) . Best expected value should be 0,8. This could come from a larger active surface of the diode than expected.

☞ The NEP for bias equal to 14V (last row) is higher than expected. Optimization on thermal cooling and thermal noise attenuation is necessary to get closer to simulated values.
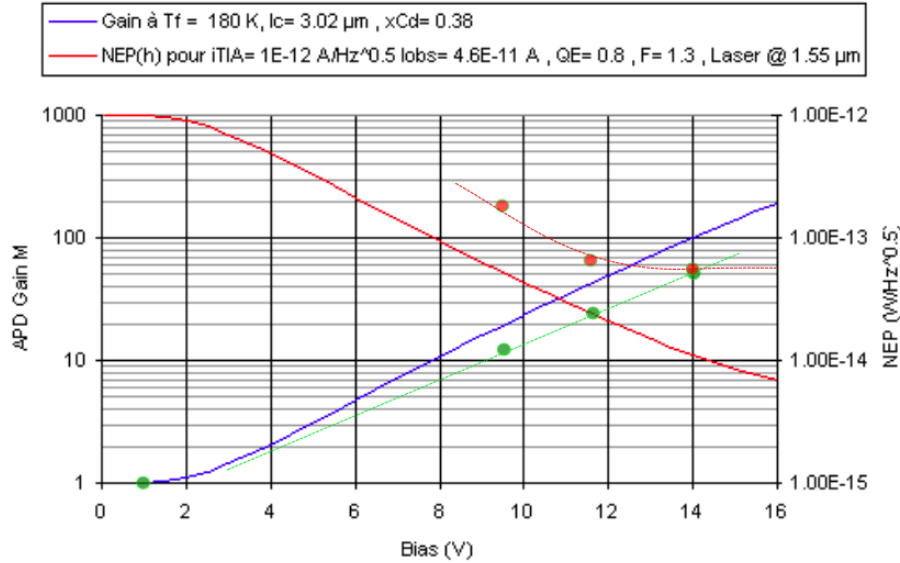

Figure 14: Estimation of NEP and Gain as functions of bias - simulated results - and experimental points. In green are the gain experimental points and in red the NEP experimental points. We notice that the thermal photonic radiations noise limits the NEP over a reverse bias of 12V. The gain is also a bit lower than expected but as it is computed from the power coming out of the laser diode, the thermal photonic radiations could also account for this difference.

Conclusion. HgCdTe APDs performances are close the predicted one. However the system reveals to be extremely sensitive to temperature and background radiations. As a consequence its performances will strongly rely on quality of others components : cooling system for the APD, cooling of the local environment, eventual filter for background radiation, etc.

5 Instrumental simulator for DIAL lidar

The DIAL lidar principles and equations have been presented in the previous sections. A basic instrumental simulator has been implemented and is presented in this section. The aim for such a simulator is to estimate the performances of a future lidar system for different technological choices and configurations.

5.1 Description of the simulator

5.1.1 Atmospheric model

We use ISA[14] temperature-pressure vertical profiles. Following [5], we derive $\alpha_{s,m}$ - the molecular extinction due to scattering coefficient - from temperature T and pressure P.

$$\alpha_{s,m}(\lambda) = 1,17 \left(\frac{\lambda}{0,55} \right)^{-4,09} \cdot \left(\frac{P}{1013} \frac{288}{T} \right) 10^{-5}$$

and the molecular backscattering coefficient $\beta_{\pi,m}$:

$$\beta_{\pi,m} = \frac{3}{8\pi} \alpha_{s,m}$$

Moreover $\alpha_{s,p}$ - the particular extinction due to scattering coefficient - is arbitrarily selected. We only want to reach the right order of magnitude that is 10^{-4} m^{-1} and model the shape of the atmospheric boundary layer (ABL). That is that the particular mixing ration drops over the summit of the ABL (around 1500m).

We will consider the absorption only due to the molecular absorption of the gas of interest, ie CO_2. Indeed, around 2 μm the absorption is negligible for O_2, N_2. Moreover, the choice for not considering the aerosol absorption is that we do not need to discriminate between particular extinction due to absorption on the one hand, and due to scattering on the other hand. Thus we only keep one coefficient $\alpha_{s,p}$. Finally the total extinction coefficient $\alpha_e = \alpha_{a,CO_2} + \alpha_{s,m} + \alpha_{s,p}$.

5.1.2 CO2 vertical distribution

We assume that CO2 mixing ratio vertical distribution follows :

$$N_{CO_2} = 10 \cdot 10^{-6} \cdot \frac{\alpha_{s,p}}{\max_z(\alpha_{s,p})} \cdot \frac{P}{kT} + 390 \cdot 10^{-6} \frac{P}{kT}$$

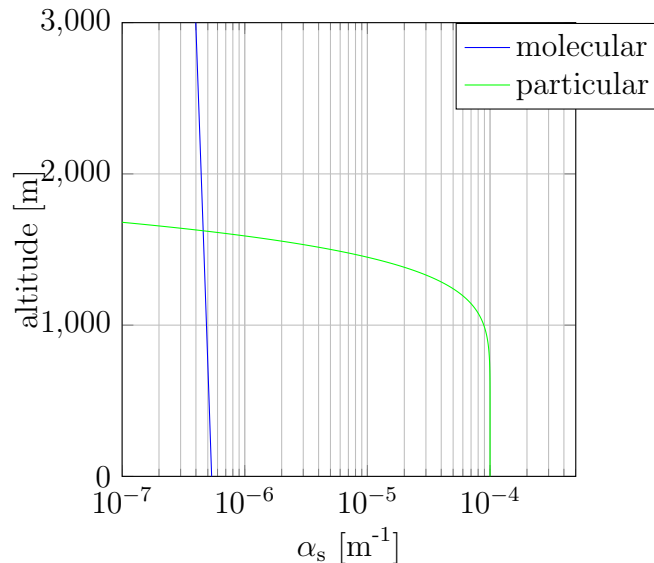[14]International Standard Atmosphere

Figure 15: Model for molecular and particular profiles in the atmosphere.

This modeling basically assumes that carbondioxide mixing ration is almost constant whatever the altitude (around 390 ppm). We only added a small dependance to ABL structure (10 ppm). We use GEISA[15] spectroscopic database to derive CO2 absorption band features.

5.1.3 Laser pulse modeling

We assume purely monochromatic laser source (λ) and pulses whose parameters are E - the energy per pulse - and τ - the pulse length. A natural question is : what is the benefit of modeling the pulse with a real temporal shape compared to the dirac model (basically with peak power E/τ), which is far more simple to handle from a numerical point of view. We have performed the comparision for gaussian temporal shape (see Fig 16). Mathematical details are provided in Complement 1.

We notice that beyond fifty meters, the difference is negligible. As a consequence, we will only work the dirac model in the following.

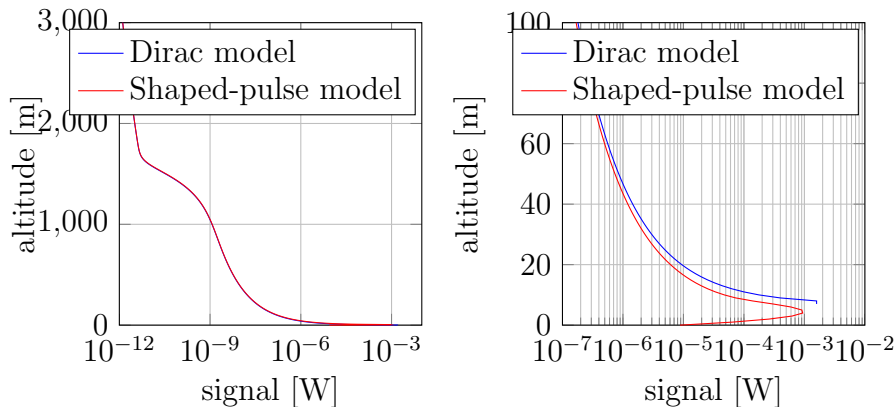[15]see `http://ether.ipsl.jussieu.fr/etherTypo/?id=950`

Figure 16: Backscattered signal. Comparison between dirac pulse model and gaussian pulse model.

5.2 Calibration of the simulator

As mentioned in the first section, an important parameter for any lidar system is the overall optical efficiency. To get a good idea of the achievable efficiency, we will use results presented in the literature and calibrate our simulator with them.

CO$_2$ measurements at 1,6 μm in direct detection were presented at the 5th International workshop on CO$_2$/CH$_4$ remote sensing (Kyushu University, March 2012). These results from Y.Shibata, C.Nagasawa and M. Abo are presented in Fig 17.

Regarding the vertical structure in Fig 17, it is clear that the top of the ABL is located around $z = 2200$m. To calibrate the simulator, we first adjust our atmospheric model so that the mixing ration of particles drops at 2200m. Then - considering that the backscattered signal over 2200m is only due to molecular scattering - we adjust the optical efficiency of the system. Finally, we use the values of backscattered signal below 2200m to adjust the particular scattering coefficient. The results are plotted in Fig 18.

Recall that the goal of our calibration was to find the following parameters : K_{opt}, the overall optical efficiency, and $\alpha_{s,p}$, the scattering coefficient due to particles. Using Shibata's measurements, we derived :

$$K_{opt} = 5 \cdot 10^{-3}$$

and

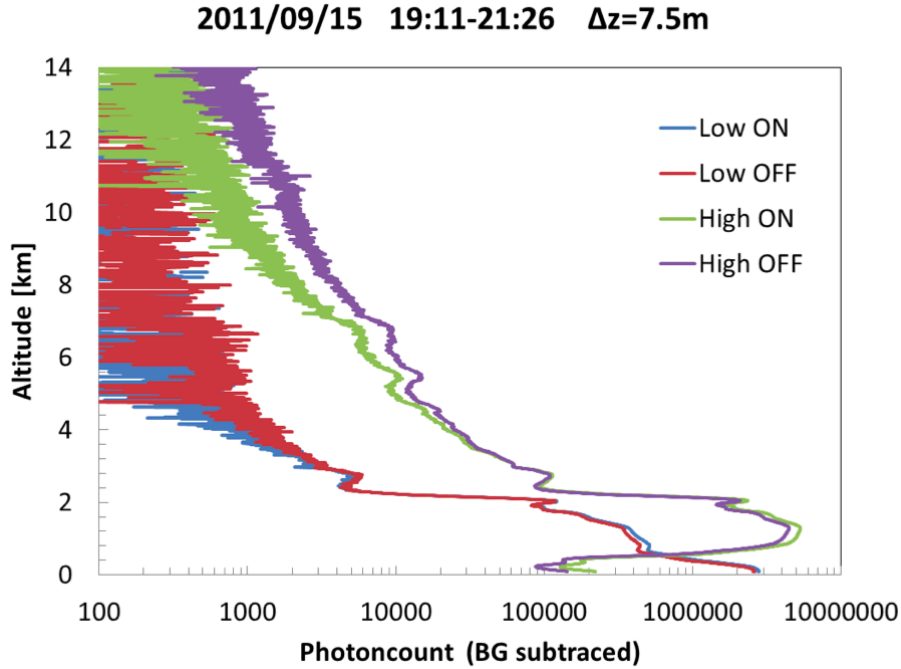$$\alpha_{s,p} = 5 \cdot 10^{-5} \text{m}^{-1}$$

27

Figure 17: Backscattered signal at wavelength ON and OFF. The high mode corresponds to the use of a big telescope (aperture 50 cm) and a quantum efficiency of 8%. On the contrary the low mode corresponds to the use of a small telescope (aperture 20 cm) and a quantum efficiency of 2%. In both cases the pulse energy is 7 mJ and the PRF 250 Hz. Taken from Shibata et al. (2012)

Remarks.

☞ For low altitude, the simulator does not follow experimental data. The reason for that is that we have not model a phenomenon called overlapping. The point is that any telescope has a field of view and that the laser radiation enters the telescope field of view (FOV) beyond some altitude $z_{overlap}$. As the interesting case is the situation where the laser beam is fully in the FOV we did not try to model overlapping so much.

☞ Around 1,6 μm, the CO_2 absorption cross section intensity is rather low. For this reason it is difficult to distinguish the ON and OFF signals in Low mode. We will see more difference around 2μm.

☞ Given Δz as accumulation range, we derive $\Delta t := \frac{2\Delta z}{c}$ the corresponding accumulating time. Now over the period T, $T \times PRF$ shots are performed, meaning that the total accumulation of pho-
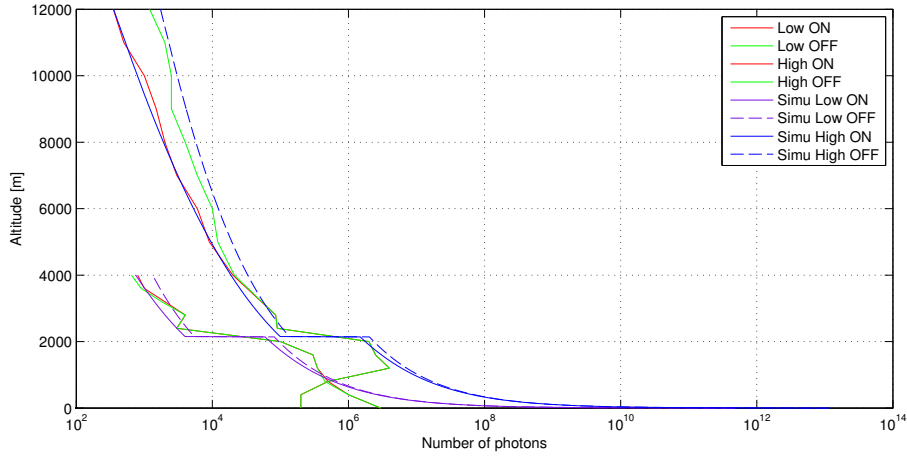
Figure 18: Experimental data are roughly reproduced and compared to the simulations. The calibration was made for High mode data. That is to say that simulations for Low mode do not use Low mode experimental data. Notice that curves stop when signal gets drowned into noise.

tons during T is given by :

$$P \cdot T \cdot PRF \cdot \Delta t \cdot \frac{\lambda}{hc} \cdot \eta$$

5.3   Expected signal at 2μm

Thanks to calibration done in the previous section, we are able to compute the expected backscattered signal (in terms of counted photons for example) for a DIAL lidar with parameters identical to COWI ones. We also assume that we have a HgCdTE APD working fine with $\eta = 0.8$. The results are presented in Fig 19. Notice the intensity of absorption at 2 μm.

Improvements in the number of collected photons are imputable to :

☞ a higher energy per pulse

☞ a higher pulse repetition frequency
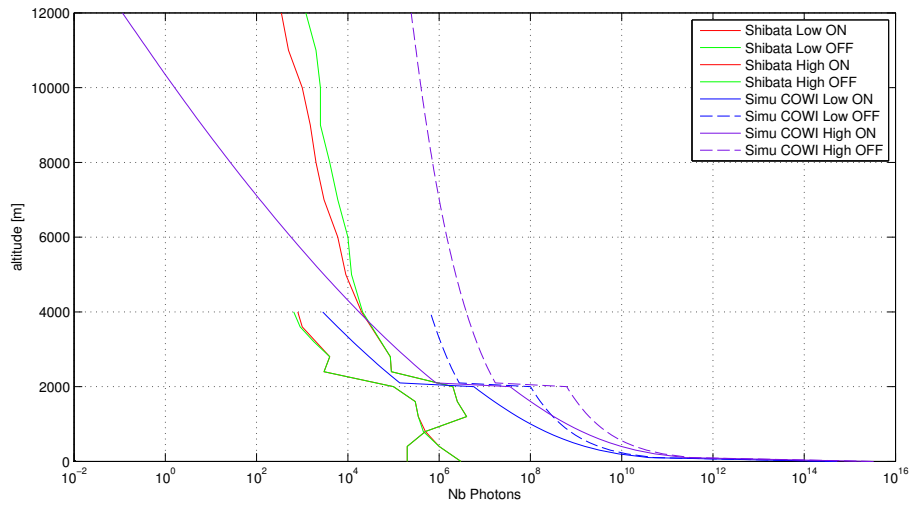
☞ a higher quantum efficiency.

Figure 19: Using Shibata's setups - ie for two different telescopes - cowi laser features and HgCdTe APDs efficiency, we plot the simulated number of backscattered photons that are converted by the detector over the same accumulating period

6 Conclusion and prospects

Experiments on HgCdTe APDs have confirmed their outstanding abilities to detect low intensity signals. However other challenging issues such as reliable cooling and filtering of parasite radiations have to be solved to reach the full potential of these detectors. On top of that, further characterization such as spatial homogeneity and linearity of the gain at 2 μm has to be carried out to guarantee the trustability of measurements. These actions will be undertaken in the following of my PhD.

Regarding lidar applications, the instrumental simulator presented in this work will be an essential tool to understand the results of the experiments that will be performed in the coming months. Indeed it enables to predict the expected signal given technological choices and specific constraints related to different applications. For example, in case of polluting source monitoring, if we choose λ_{ON} at the top of the absorption line, the absorption will be very important and the range of measurements will be limited. In such a case the simulator can be used to infer a suitable spectral position. Another important point is the expected precision on measurement given technological choices. For satellite applications for example, as it is not possible to accumulate so many measurements over the same area, it is crucial to design the lidar according to required precision.

Complement 1

Continuous case   Assume the pulse temporal shape is given by a time function $t \to f(t)$. We consider the propagating time space function $(t, z) \to \phi(t, z)$. Assuming constant speed propagation along z axis we can write :

$$\phi(t, z) = \phi(t - t_0, z - ct_0)e^{-\int_{z-ct_0}^{z} \alpha_e(x)dx}$$

We finally assume that

$$\phi(t, 0) = f(t)$$

We want to know the amplitude seen by the detector due to backscattering. We note it $D(t)$ assuming the detector surface is located at $z = 0$. Considering what arrive on the detector at time t, we have to sum all the contributions from signal coming come (t', z') such that $z' = c(t - t')$. We get

$$D(t) = \int_{(t',z')/z'=c(t-t')} z'^{-2}\beta_\pi(z')\phi(t', z')e^{-\int_0^{z'} \alpha_e(x)dx}dz'dt'$$

This was the trickiest part of the reasoning. Indeed it is not that esay at first sight to write it properly. Now we can just substitute with previous equations. First we choose z' as variable in the integral since the backscattering coefficient is a function of altitude.

$$D(t) = \int_0^\infty z'^{-2}\beta_\pi(z')\phi\left(t - \frac{z'}{c}, z'\right)e^{-\int_0^{z'} \alpha_e(x)dx}dz'$$

Now we want to express ϕ as a function of f. Introduce t_0 such that $ct_0 = z'$. Following previous equation we get :

$$D(t) = \int_0^\infty z'^{-2}\beta_\pi(z')f\left(t - \frac{2z'}{c}\right)e^{-2\int_0^{z'} \alpha_e(x)dx}dz'$$

The final point to mention is that f is non zero only between 0 and τ where τ is the pulse duration. Finally

$$D(t) = \int_{c(t-\tau)/2}^{ct/2} z'^{-2}\beta_\pi(z')f\left(t - \frac{2z'}{c}\right)e^{-2\int_0^{z'} \alpha_e(x)dx}dz'$$

Discrete case We focus now on what happens when assuming Δt, Δz finite resolution. Basically Δz is not choosable since any data set will be given for a certain altitude vector. Therefore we will choose $\Delta t = \frac{2\Delta z}{c}$. The factor 2 is added to simplify the following calcula. Finally we choose $\tau = k\Delta t$ and it comes

$$D(t = l\Delta t) = \sum_{m=l-k}^{l} \frac{1}{(m\Delta z)^2}\beta_\pi(z = m\Delta z)f((l-m)\Delta t)e^{-2\sum_{n=1}^{m}\alpha_e(m)\Delta z}\Delta z$$

which can be written

$$D(l) = \sum_{m=l-k,m\geqslant 0}^{l} \frac{1}{m^2(\Delta z)^2}\beta_\pi(m)f(l-m)e^{-2\sum_{n=1}^{m}\alpha_e(m)\Delta z}\Delta z$$

We have added a condition $m \geqslant 0$, which is a side effect that could also be added in continuous case.

References

[1] Borge Vinter Emmanuel Rosencher. *Optoelectronics.* Cambridge University Press, 2004.

[2] FACTS. *Future Atmospheric Carbon Testing from Space.* IPSL study ordered by the European Space Agency, 2004.

[3] Fabien Gibert. *Télédétection du CO_2 Atmosphérique par lidar DIAL doppler hétérodyne à 2 μm.* Ecole Polytechnique PhD, Institut Pierre Simon Laplace, Laboratoire de Météorologie Dynamique, 2005.

[4] Raymond Measures. *Laser Remote Sensing, Fundamentals and Applications.* Krieger Publishing company, Malabar, Florida, reprint edition, 1992.

[5] P.H.Flamant. Lidars atmosphériques et météorologiques - principes fondamentaux. *Techniques de l'ingénieur*, (e4310), august 2008.

[6] Johan Rothman. Hgcdte apds for imaging and remote sensing. *OPTRO 2014*, january 2014.

[7] Claus Weitkamp. *Lidar - Range-resolved Optical Remote Sensing of the Atmosphere.* Springer, 2005.